J. Fluid Mech. (2001), *vol.* 429, *pp.* 155–185. Printed in the United Kingdom

Shock unsteadiness in a reattaching shear layer

By J. POGGIE[1] AND A. J. SMITS[2]

[1]Air Force Research Laboratory, AFRL/VAAC, 2210 Eighth St, WPAFB,
OH 45433-7521, USA

[2]Department of Mechanical and Aerospace Engineering, Princeton University, POB CN5263,
Princeton, NJ 08544-5263, USA

(Received 26 August 1999 and in revised form 25 July 2000)

The origin of shock unsteadiness in a Mach 2.9 turbulent reattaching shear layer was investigated experimentally using temporally resolved flow visualization and measurements of wall pressure fluctuations. In this flow, the separation point of a turbulent boundary layer is essentially fixed at a backward-facing step, and the reattachment point is free to move along a ramp. In order to examine the influence of disturbances originating in the incoming shear layer, artificial disturbances were introduced into the flow through steady air injection in the vicinity of separation. The effect on the reattachment shock system was dramatic: the intensity of the pressure fluctuations and the amplitude of the shock motion increased substantially, and power spectra of the pressure fluctuations showed a distinct shift to lower frequency. The spectra collapsed onto a common curve in non-dimensional coordinates based on a length scale derived from two-point cross-correlations of the flow visualization data and a convection velocity derived from cross-correlations of the pressure measurements. The data were compared to a theory developed by Plotkin (1975), which is based on perturbation of a shock by random fluctuations in the incoming turbulent flow. Plotkin's model mimics the manner in which relatively broad-band perturbations in the incoming turbulent flow lead to relatively low-frequency motion of the separation bubble and its associated shock system. It is an excellent fit to separation shock motion, such as that generated in a blunt fin flow (briefly illustrated here). In the present shear layer flow, this low-frequency motion was detectable in the spectra near reattachment, but contained considerably less energy relative to the shock motions caused by direct perturbations by the incoming turbulent structures. These results indicate that the shock motion in the reattaching shear layer is primarily caused by organized structures in the incoming turbulent flow.

1. Introduction

The mechanisms of shock unsteadiness in separated turbulent boundary layer flow have been a topic of extensive research, motivated primarily by the need to mitigate aircraft fatigue loading caused by the intense fluctuations in wall pressure and heat flux that accompany shock oscillation. An added emphasis has been placed on this class of flows recently, as a consensus has evolved that resolving the large-scale shock unsteadiness is necessary for accurate computations of the mean flow (Hunt & Nixon 1995; Dolling 1998; Urbin, Knight & Zheltovodov 1999). Although shock unsteadiness was noted in early flow visualization experiments on separated turbulent flows, the first systematic study of this problem was carried out by Kistler (1964), who measured wall pressure fluctuations in a supersonic forward-facing step flow. Kistler observed an intermittent wall pressure signal in which fluctuations due to turbulence in the incoming boundary layer and separation bubble were modulated by rapid pressure jumps associated with the motion of the separation shock back and forth across the transducer. This pattern has since been observed experimentally in a wide variety of separated supersonic flows over two- and three-dimensional test configurations (see Dolling 1993).

The shock motion has a broad spectral content, but appears to contain two characteristic scales: one because of perturbation of the shock by organized structures in the flow turbulence and the other because of relatively large-scale, low-frequency expansion and contraction of the separation bubble (Poggie & Smits 1997). The shock motion may be driven in part by cyclic vortex shedding analogous to that observed in low-speed separated flows (Eaton & Johnston 1982; Driver, Seegmiller & Marvin 1987; Thomas 1987; Visbal 1991), and also by turbulence in the separation bubble and in the incoming flow (Bogar 1986; Erengil & Dolling 1993; Brusniak & Dolling 1994).

The δ-scale shock motion has been observed directly (Smith 1989; Smith *et al.* 1991; Forkey *et al.* 1993; Wu, Lempert & Miles 2000) using a planar visualization technique based on Rayleigh scattering. Images obtained with this technique show that the shock is distorted, and often split, by organized structures as they convect into the separation zone. Difficulty in seeding the separation zone with scattering particles has precluded visualization of the large-scale shock motion with laser scattering techniques. Kussoy *et al.* (1988), however, have observed the expansion and contraction of the separation bubble using cinematic shadow photography in a configuration where the line of sight averaging inherent in this technique was minimized.

Profiles of the intensity of pressure fluctuations (Dolling & Murphy 1983) and heat transfer fluctuations (Hayashi, Aso & Tan 1989; Shifen & Qingquan 1992) along a streamwise line at the wall of a separated boundary layer in compressible flow typically show two distinct maxima: one just upstream of the mean separation line and one near the mean reattachment line. These peaks may be an order of magnitude above the fluctuation levels in the incoming turbulent boundary layer flow. Conditional averaging has shown that, in many flows, the peaks are caused by motion of the two legs of a lambda shock system (the separation and reattachment shocks) as the separation bubble expands and contracts (Erengil & Dolling 1991; Brusniak & Dolling 1994).

Most research has focused on the motion of the separation shock, with relatively little emphasis on reattachment shock unsteadiness. To address this lack of data, Shen, Smith & Smits (1993) investigated the wall pressure fluctuations in a flow where the separation point was essentially fixed at a backward-facing step, but the reattachment point was free to move along a ramp. The character of the shock unsteadiness in the reattaching flow was found to be substantially different from that of a typical separating flow. In particular, less of the spectral content of the pressure fluctuations was concentrated at low frequencies, and the characteristic intermittent pressure signal was not observed. These features were, however, similar to measurements made near unsteady reattachment in other supersonic turbulent flows (Dolling & Murphy 1983; Selig *et al.* 1989).

The present study was undertaken to extend the work of Shen *et al.*, and to search for mechanisms which might be responsible for shock unsteadiness in the reattaching shear layer. The fluctuations in wall pressure caused by the motion of the reattachment shock system were measured, and the flow was visualized using a laser scattering technique. In order to examine the influence on the reattachment shock system of disturbances originating in the incoming shear layer, experiments were conducted in which artificial disturbances were introduced into the flow through steady air injection in the vicinity of separation.

1.1. *Theoretical model*

The primary mechanism for shock oscillation in the reattaching shear layer configuration is believed to be perturbation by disturbances in the incoming turbulent flow. A theoretical model for this process has been developed by Plotkin (1975).

Plotkin assumed that a stable location exists for the shock, the position where the shock would sit if no disturbances were present in the incoming flow. As an organized structure convects into the vicinity of the shock, it changes the jump conditions across the shock, and causes it to move away from the equilibrium position. After the eddy passes, the shock obtains a velocity in its new environment that tends to return it toward the equilibrium position.

For simplicity, Plotkin considered only a one-dimensional model for oscillation in the direction parallel to the wall. The shock velocity $\dot{x}$ was taken to be the superposition of a random forcing function u and a restoring velocity that is proportional to the displacement x of the shock from its equilibrium position:

$$\dot{x} = u(t) - x/\tau_R. \tag{1.1}$$

Here t is time, and τ_R is a constant (with units of time) specifying how rapidly the shock recovers from a perturbation. The variables x and u are defined to have zero mean.

Plotkin considered the random function u to represent convection of the shock by velocity fluctuations in the boundary layer. This function is probably better viewed as the shock velocity induced by changes in the jump conditions due to turbulent fluctuations. For linearized jump conditions, u would be proportional to the velocity fluctuations in the boundary layer. The restoring term in (1.1) represents the shock velocity induced by changes in the local jump conditions due to displacement of the shock from its equilibrium location. The time constant τ_R is expected to be determined primarily by the characteristics of the separation bubble flow.

For a given history of velocity perturbations, (1.1) can be solved to give the resulting time-history of shock position. Assuming that $x(0) = 0$, the solution can be put in the form

$$x = \mathrm{e}^{-t/\tau_R} \int_0^t u(\xi)\mathrm{e}^{\xi/\tau_R}\, \mathrm{d}\xi. \tag{1.2}$$

Plotkin used (1.2) to relate the statistical properties of the shock motion to those of the fluctuations in the turbulent boundary layer, noting an analogy to linearly damped Brownian motion.

An important parameter characterizing both the velocity fluctuations and the consequent shock motion is the integral time scale of the auto-correlation function $R(t)$. The integral time scale is defined as

$$\tau_i = \int_0^\infty R_i(\tau)\, \mathrm{d}\tau, \tag{1.3}$$

where i is replaced by u, x, or p to indicate the auto-correlation of the fluctuations in the turbulent boundary layer, the shock position, or the wall pressure fluctuations. The auto-correlation function is defined in the usual manner for time-series data.

Assuming that the shock response is much slower than the turbulent fluctuations ($\tau_R \gg \tau_u$), Plotkin found an approximate expression for the mean-square shock excursion at large time ($t \gg \tau_u$):

$$\overline{x^2} = \overline{u^2}\,\tau_u \tau_R, \tag{1.4}$$

where an overbar indicates a time average. From the same assumptions, he also derived the following simplified form for the auto-correlation of the shock position:

$$R_x(t) = \mathrm{e}^{-t/\tau_R}. \tag{1.5}$$

At this level of approximation, the auto-correlation of the shock position is independent of the detailed statistical properties of the boundary layer turbulence, and the integral time scale of the shock position is the same as the time constant of the restoring velocity: $\tau_x = \tau_R$.

Plotkin went on to assume that the pressure distribution induced by the oscillating shock can be approximated by the mean pressure distribution translated to the instantaneous shock position. Expanding the mean pressure distribution in a Taylor series about the mean shock location, and retaining terms to first order, he showed that the mean-square fluctuating pressure is proportional to the mean-square shock excursion:

$$\overline{p'^2} = \left(\frac{\partial \bar{p}}{\partial x}\right)^2 \overline{x^2}, \tag{1.6}$$

where a prime indicates the fluctuating component of the pressure. (Recently, Brusniak & Dolling (1996) have successfully used a related approximation to predict fluctuating loads due to separation shock oscillation.) Further, the auto-correlation of the pressure fluctuations is the same as that of the shock position: $R_p(t) = R_x(t)$ and $\tau_p = \tau_x = \tau_R$. He then calculated the one-sided power spectrum of the pressure fluctuations from the Fourier transform of the auto-correlation:

$$G(f) = \frac{4\overline{p'^2}\tau_p}{1 + (2\pi f \tau_p)^2}, \tag{1.7}$$

where f is the frequency, and the approximation requires that $f \ll 1/(2\pi\tau_u)$. Plotkin also assumed that the integral time scales were proportional to a characteristic boundary layer time scale δ/U_e, where δ is the local boundary layer thickness and U_e is the mean velocity at the boundary layer edge.

These results suggest two ways of plotting non-dimensional power spectra. For comparison to the basic theory, plotting the form $G(f)/(\overline{p'^2}\tau_p)$ against $2\pi f \tau_p$ is most natural, whereas $G(f)U_{\mathrm{ref}}/(\overline{p'^2}\delta_{\mathrm{ref}})$ vs. $f\delta_{\mathrm{ref}}/U_{\mathrm{ref}}$ may be a suitable form to collapse data obtained under different experimental conditions.

Alternative treatments of the interaction of organized structures with a shock have used linearized versions of the Euler equations and shock jump conditions to predict the distortion of the shock shape and the amplitude of downstream disturbances caused by a small oncoming perturbation. (See, for example, Erlebacher & Hussaini (2000) and the references therein.) Plotkin's work is better viewed as a conceptual model of the unsteadiness of the shock and separation bubble, than as a linearized shock evolution equation. Whereas a linearized theory would predict the spectrum of shock unsteadiness to be essentially the same as that of the incoming turbulence, Plotkin's model is able to mimic the way in which relatively broad-band perturbations in the incoming flow lead to relatively low-frequency motion of the separation bubble and its associated shock system. In this way, the model incorporates some of the

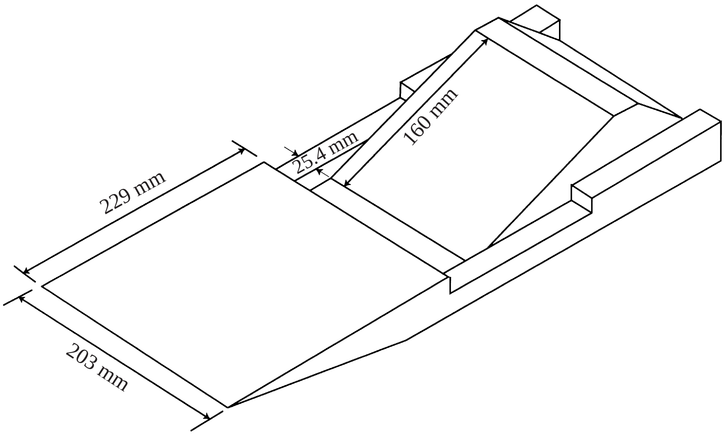

Figure 1. Diagram of the experimental model. Adapted from Baca (1981).

nonlinear aspects of the interaction of organized structures and a shock in a separated turbulent flow.

2. Experimental methods

The experiments were carried out in the Princeton University Gas Dynamics Laboratory Mach 3 blow-down wind tunnel. High-pressure air is supplied to the facility by as many as five Worthington 75 kW four-stage compressors. The compressed air passes through a chemical drying system, and is stored at pressures of up to 20 MPa in four tanks with a total capacity of 57 m^3. An hydraulically controlled valve regulates the tunnel stagnation pressure as the air flows from the storage tanks into the settling chamber. The experiments were carried out in the first of the wind tunnel's three 902 mm long test sections, which has a square cross-section of 203 mm by 203 mm. The pressure in the settling chamber was maintained at 0.69 ± 0.03 MPa for all experiments, and the free-stream Mach number was 2.92 ± 0.01. In a two-minute typical run, the stagnation temperature was initially 290 K and dropped by about 8%. Typical unit Reynolds numbers were on the order of $\rho_\infty U_\infty / \mu_\infty = 6.5 \times 10^7\ \mathrm{m}^{-1}$.

The experimental configuration for the reattaching shear layer is illustrated in figures 1 and 2. The experimental model was originally designed by Baca (1981). In this flow, a Mach 2.9 turbulent boundary layer forms on a flat plate and detaches at a backward-facing step. As a result, a free shear layer forms over a region of recirculating flow. The shear layer reattaches on a 20° ramp, passing through an oblique shock system, and a turbulent boundary layer develops on the ramp downstream.

Surveys of the basic properties of the flow field were performed in earlier experimental programmes at the Princeton Mach 3 wind tunnel for the same geometry and test conditions studied here (Baca 1981; Horstman *et al.* 1982; Settles *et al.* 1982; Hayakawa, Smits & Bogdonoff 1984; Shen *et al.* 1993). Similar configurations have been investigated in other facilities (Samimy, Petrie & Addy 1986; Samimy & Addy 1986; Smith & Dutton 1996). For brevity, previously published details of the undisturbed flow field are omitted here. Settles *et al.* (1982) present velocity profiles (based on Pitot pressure, static pressure, and total temperature probe measurements) of the incoming turbulent boundary layer, the free shear layer, and the redeveloping boundary layer on the ramp. Profiles of the mean and root-mean-square mass flux, based on hot-wire measurements, were presented by Hayakawa *et al.* (1984), and fluc-

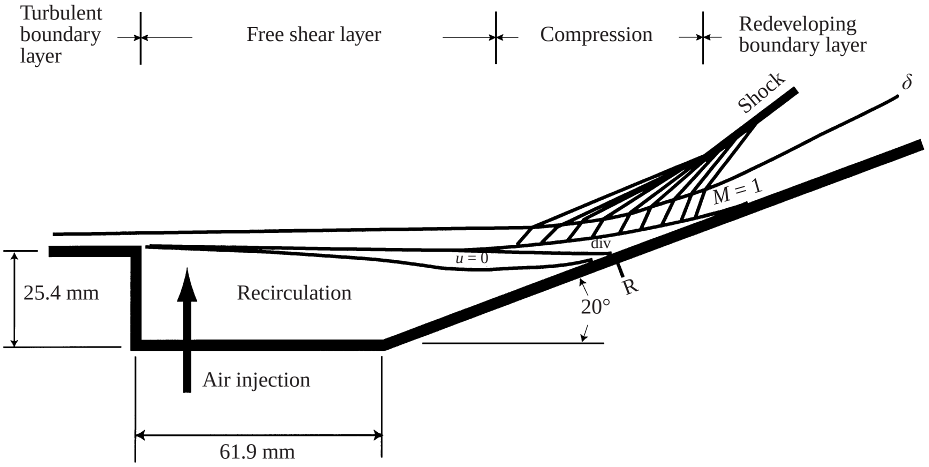

FIGURE 2. Sketch of a cross-section of the mean flow field. 'R' – reattachment location, 'δ' – boundary layer/shear layer edge, '$M = 1$' – sonic line, 'div' – dividing streamline, '$u = 0$' – boundary of recirculating region. Adapted from Baca (1981).

tuating pressure measurements were made by Shen *et al.* (1993). Additional details can be found in Baca (1981) and Poggie (1995).

These measurements have indicated that a zero-pressure-gradient equilibrium turbulent boundary layer is present in the vicinity of the backward-facing step with a thickness of about $\delta_s = 3$ mm (based on the location of 98% of the free-stream Pitot pressure) and a momentum thickness Reynolds number of about 10^4. Due to the position of the reattachment ramp, the boundary layer separates at the 25 mm step with only a very small change in flow direction (in all cases less than 1.5°, based on the pressure ratio across the step and measurements from schlieren photographs of the angle of the shear layer's upper edge). The mean velocity profiles of the resulting free shear layer become self-similar about $18\delta_s$ (58 mm) downstream of the step, where the nominal convective Mach number (Papamoschou & Roshko 1988) is about 1.1 and the growth rate is in good agreement with data from other compressible, turbulent mixing layer experiments (see Horstman *et al.* 1982). Surface flow visualization data show a nominal mean reattachment line 67 ± 1 mm up the 20° ramp; this position corresponds closely to the location of the shear-layer dividing streamline inferred from mean velocity measurements (Baca 1981). The boundary layer on the ramp is strongly perturbed near reattachment; it approaches, but does not reach, an equilibrium condition farther downstream.

In order to provide optical access to the flow, the experimental model was modified by Shen *et al.* (1993) from the original design of Baca. The cavity of the model was fitted with removable inserts so that the height of the sidewalls (the walls that form the ends of the cavity in the spanwise direction) could be set at either 15.9 mm or 25.4 mm (see figure 1). The experiments reported here were carried out with the sidewall inserts and the aerodynamic fences on the sides of the ramp removed. All the mean and fluctuating pressure measurements were repeated for both the case with the fences and inserts in place and for the case with them removed (Poggie 1995). The alterations of the model were found to have a slight quantitative, but no qualitative, effect on the flow field. In particular, a slight deflection angle was introduced where the flow detached from the backward-facing step, changing the ratio of the pressure on the plate to that in the cavity from 1.01 to 1.04.

2.1. *Flow visualization*

A series of experiments was carried out in which the reattachment shock system was visualized using Rayleigh scattering from nanometer-scale contaminant particles in the flow. Illumination was provided by an ultraviolet laser beam focused into a thin sheet in the wind tunnel. The experimental arrangement used optics with a UV-coating, and quartz windows provided optical access to the tunnel test section. Two lasers were used in the course of the experimental program: a Lambda-Physik argon fluoride laser with a wavelength of 193 nm and a frequency-quadrupled Continuum Nd : YAG laser with a wavelength of 266 nm. Both lasers provided a pulse on the order of several nanoseconds in duration at a repetition rate of 10 Hz, and delivered 20–50 mJ of energy per pulse. A double-intensified ITT CID (charge integrated device) camera recorded the light scattered from the laser sheet. The camera had a resolution of 388 by 244 pixels, and the light intensifier had a resolution of 180 lines. The video data were recorded on VHS video tape, and later digitized for analysis.

Additional experiments were carried out in which the Continuum Nd : YAG laser was used in double-pulse mode, producing pairs of pulses separated by an interval of 12 to 60 μs (see Cogne *et al.* 1993; Forkey *et al.* 1993). For this case, two cameras, gated to record the two pulses in sequence, were mounted on opposite sides of the wind tunnel and aligned to record the same field of view. In order to ensure that the cameras were properly aligned, an image of a precision grid in the test section was recorded before and after each wind tunnel run. The accuracy of positioning was found to be within 1% of the width (58 mm) of the field of view in all the tests.

The scattering signal is believed to be dominated by Rayleigh scattering from a uniform fog of clusters of H_2O, CO_2, or O_2 molecules that form in the free-stream flow as the air cools in the expansion through the wind tunnel nozzle (see Wegener & Pouring 1964; Shirinzadeh, Hillard & Exton 1991). Observations from past work have indicated that the scattering intensity (and thus the particle number density) tends to follow the air density, except where the temperature reaches a level high enough to vaporize the contaminant particles (Smith *et al.* 1991; Nau 1995). Since the molecular constituents of air have a much smaller scattering cross-section than the relatively larger particles, images of high-temperature regions of a flow may therefore appear dark.

For free-stream temperatures on the order of 100 K, the fluid near the instantaneous edge of a Mach 2.9 turbulent boundary layer or free shear layer has a temperature high enough to vaporize the molecular clusters, and a sharp vaporization interface reveals organized structures in the two turbulent shear flows. For relatively weak shocks, the Rayleigh scattering images show an increase in scattering intensity due to the shock density jump, but for stronger shocks, the images show a marked decrease in scattering intensity across the shock, due to vaporization of the scattering particles.

A body of evidence has been accumulated that indicates that the scattering images have accurately portrayed many of the physical features of a turbulent boundary layer, a turbulent mixing layer, and several shock-wave/boundary-layer interactions studied in the Princeton supersonic wind tunnel (Poggie & Smits 1996). In particular, quantitative measures of the scale, orientation, and speed of large-scale organized structures derived from a statistical analysis of scattering images of the turbulent boundary layer and turbulent mixing layer agree well with results obtained in the same flows using hot-wire anemometry. Further, Nau (1995) has examined simultaneous hot-wire and Rayleigh scattering measurements of the turbulent boundary layer, and found a strong correlation between traces of the hot-wire signal and the corresponding scattering profiles.

2.2. *Measurements of wall pressure fluctuations*

Static pressure measurements were made with miniature differential pressure transducers manufactured by Kulite Semiconductor Products (model XCQ-72-062-25D). Past work with these transducers has shown that they have an acceptable frequency response up to about 50 kHz under the present test conditions (e.g. see Spina 1988). The transducers were calibrated statically at the operating temperature. Previous studies, and checks made before and after wind tunnel runs, have shown that the calibration is consistently linear and repeatable.

The transducers were mounted in a block that could be positioned at different streamwise positions along the reattachment ramp. The spacing between the transducers was 5.1 mm, and they were mounted 2.5 mm off the centreline of the wind tunnel. The data were taken with the block positioned in three locations. Three of the four available transducers were found to calibrate accurately, and were used to cover a range of positions between 52 and 88 mm from the start of the ramp.

The signals from the transducers were amplified, then band-pass filtered with a four-pole Butterworth filter. Typical ratios of the signal level to the electronic noise in the system are around 12 for the undisturbed boundary layer (Spina 1988), and improve for the higher intensity pressure fluctuations encountered with shock unsteadiness. The analogue data were sampled digitally with 10 bit resolution using a CAMAC (computer automated measurement and control) system from LeCroy, Inc. Three sampling rates were used: 10, 250, and 1000 kHz. In all three cases the high-pass filter was set to 10 Hz, while the low-pass filter was set to 5 kHz for the 10 kHz sampling rate, and to 80 kHz otherwise. Data were obtained simultaneously for the three channels in files of four records, each containing 24576 contiguous points per record.

2.3. *Artificial disturbances*

Artificial disturbances were introduced into the flow through steady air injection in order to investigate the effect of upstream disturbances on the unsteadiness of the shock system. Two spanwise rows of holes for air injection were added to the experimental model. One row was located 12.7 mm upstream of the backward-facing step, and the other was located 12.7 mm downstream of the step on the cavity floor. Each row was 101.6 mm long, and consisted of 33 holes, 1.6 mm in diameter. Although tests were made using a number of air injection patterns (Poggie 1995), for the experiments described here only one or three of the 33 holes downstream of the step were used, in a pattern symmetric about the centreline.

Air was supplied to the holes from the wind tunnel storage tanks, by way of a stagnation tank. A series of three pressure regulators in the supply lines brought a typical storage pressure of about 20 MPa down to the desired tank pressure of about 0.7 MPa. The blowing stagnation tank consisted of a 1.02 m length of 8 in. (203 mm) nominal diameter pipe with the ends sealed with flanges and blinds.

Air was allowed to leave the tank through sections of 1.6 mm diameter stainless steel tubing. Plastic tubing of 1.6 mm inside diameter connected the stainless steel tubing to similar tubing soldered into the holes in the experimental model.

The supply pressure was maintained at 0.69 ± 0.03 MPa for the tests reported in this paper. Results of calibration (Poggie 1995) indicate that the ratio of the mass flux through a hole to the mass flux in the free stream was on the order of $\rho_h U_h/(\rho_e U_e) = 0.07$, the momentum flux ratio was on the order of $\rho_h U_h^2/(\rho_e U_e^2) = 0.04$, and the velocity ratio was on the order of $U_h/U_e = 0.6$. (Here ρ is the density, U is the mean velocity, h indicates the hole, and e indicates the free stream.) It should be

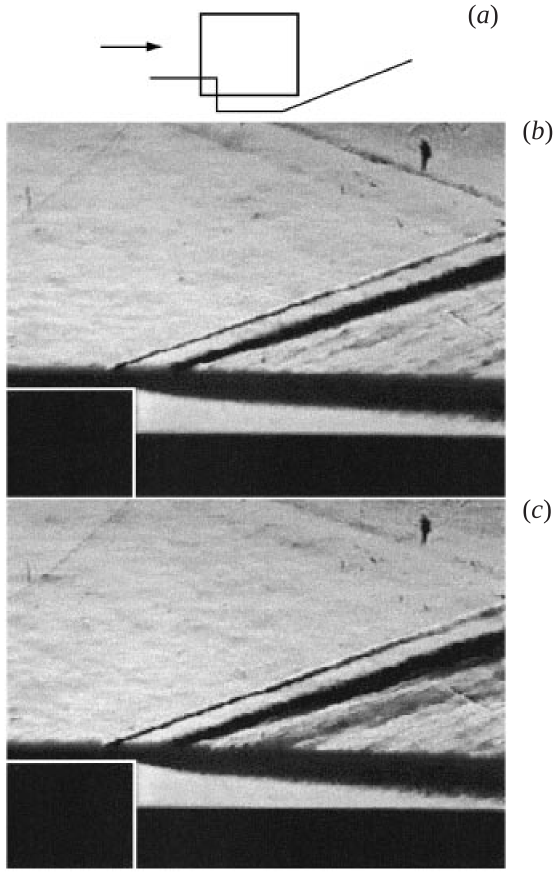

Figure 3. Schlieren photographs of the flow in the vicinity of the step. (*a*) Sketch of field of view, not to scale. (*b*) Undisturbed flow. (*c*) Air injection through three holes.

noted that these ratios refer to the values at the exit of the holes in the cavity; the jet of injected air develops over the distance between the floor of the cavity and the lower edge of the shear layer.

3. Results

3.1. *Schlieren photography*

Schlieren photographs were taken in order to provide an overview of the flow field and to demonstrate the general effects of air injection. Images were obtained for the region of the flow in the vicinity of the backward-facing step and for the region near the reattachment ramp. Example images are shown in figures 3 and 4. In each case a sketch of the field of view is shown at the top of the figure, the upper image was obtained in the undisturbed flow, and the bottom image was obtained for the case with air injection through three holes. The field of view for both the images of the region near the step and the region near the ramp is approximately 100 mm wide by 80 mm high ($10.6\delta_r$ by $7.7\delta_r$, where the boundary layer thickness in the vicinity of the mean reattachment line in the undisturbed flow is $\delta_r = 10.4$ mm).

Figure 3(*b*) shows a view of the undisturbed flow in the vicinity of the backward-facing step. Note that the sidewall blocks the bottom of the cavity from view. The

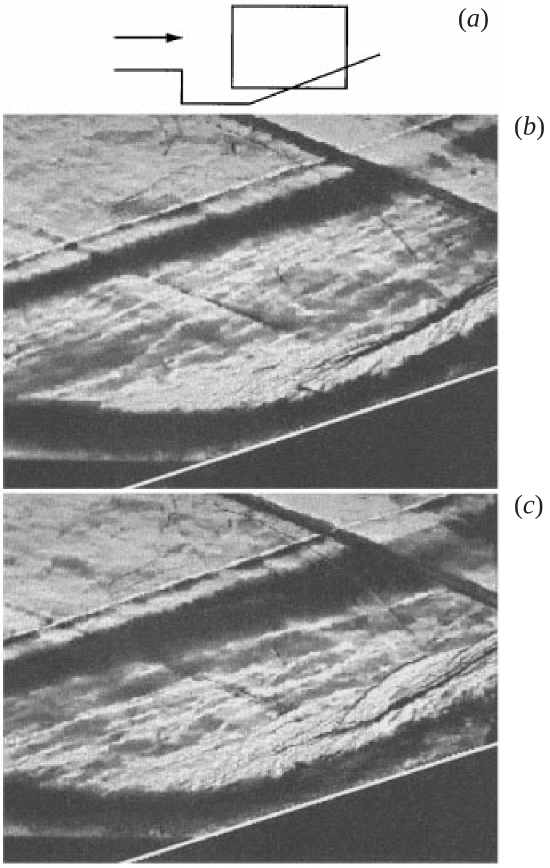

FIGURE 4. Schlieren photographs of the flow in the vicinity of the ramp. White line indicates ramp surface. (*a*) Sketch of field of view, not to scale. (*b*) Undisturbed flow. (*c*) Air injection through three holes.

uneven outer edge of the incoming turbulent boundary layer can be seen on the flat plate at the left in the field of view. A Mach wave originates at the row of holes upstream of the step. The boundary layer separates at the step with a slight change in flow direction, and an expansion fan appears centred on the edge of the backward-facing step.

The upper and lower edges of the developing free shear layer are clearly visible in the image. Since a schlieren image represents a spanwise average of the density gradients in the flow, there is relatively little indication of the large-scale structure of the turbulent flow. There are, however, waves visible emanating from the upper edge of the shear layer that are probably associated with organized structures. (The convective Mach number is supersonic for this flow.)

Figure 3(*c*) shows the effect of air injection on the flow in the vicinity of the step. (As discussed previously, the air injection holes are located in the cavity floor, 12.7 mm downstream of the step. See the sketch in figure 2.) The jets of injected air are not visible in the image because of the orientation of the schlieren knife edge. A three-dimensional shock system forms due to the jets, and is discernible as a dark curve roughly parallel to the expansion fan upstream. One surprising observation is that the shear layer shifts down (note the increased size of the expansion fan), even though mass is being added to the recirculating region, suggesting that there is enhanced entrainment of fluid from the cavity flow into the shear layer. In agreement with this observation, the shear layer also appears to thicken. Most of the change occurs on the low-speed side of the shear layer: the angle of the upper edge of the shear layer changes by less than 1°, with a correspondingly small change in the pressure ratio across the step.

The reattachment zone for the undisturbed flow case is shown in figure 4(*b*). The expansion fan centred on the backward-facing step is apparent in the free-stream flow, as are two Mach waves originating from joints in the ceiling of the test section. (The lower Mach wave is quite weak; the upper wave seems somewhat stronger, but is not detectable in the mean pressure measurements on the ramp surface, figure 11.) The free shear layer can be seen entering from the left side of the image; most of the shear layer is visible above the cavity sidewall. The highly turbulent nature of the shear layer in the vicinity of reattachment is plain, despite the spanwise averaging process inherent in the schlieren technique.

The reattachment shock system is evident in the image as the light, fan-like region above the redeveloping boundary layer. The shock system appears to be distributed in this manner for two reasons: the primary oblique shock is wrinkled along the spanwise direction, and the system is composed of a combination of a number of shocks and distributed compression waves (see the Rayleigh scattering results below).

The effect of air injection on the reattachment region is quite dramatic (figure 4*c*). The increased thickness of the shear layer and the developing boundary layer is obvious, as is the great distortion of the reattachment shock system. In the example image shown, the primary oblique shock appears to have split into several sections. The severe curvature and strong displacement of the shock system present in this image are typical of the results obtained with air injection. The increase in unsteadiness is quite spectacular in the original video recording.

3.2. *Single-pulse laser scattering*

The laser scattering technique used in the present work offers a visualization of an instantaneous planar section of the flow, revealing cross-sections of coherent structures and shock waves. A series of single-pulse laser scattering experiments was carried out to examine the scale and orientation of organized structures in several cross-sectional planes in the reattachment region of the flow, and to look for an association of these structures with shock waves. Two optical configurations were used: one with a vertical laser sheet located along the wind tunnel centreline with the field of view aligned with the reattachment ramp, and another with a horizontal laser sheet located in the outer part of the redeveloping boundary layer.

The side-view images were obtained with a relatively small field of view that allowed the resolution of smaller-scale features of the interaction of the shock system with the incoming turbulent flow. The camera was tilted 20° from horizontal, in alignment with the reattachment ramp. The field of view was approximately 26 mm wide by 20 mm high, and began 54 mm up the reattachment ramp. Sample images are shown in figure 5, with the inclined orientation of the field of view sketched at the top of the figure. The mean reattachment location for the undisturbed flow is marked ‘R’ in the figure, and the ramp surface is indicated with a line.

Figure 5(*b*) shows the undisturbed flow. The free shear layer can be seen entering from the upper left of each image, and the redeveloping boundary layer exits horizontally from the right. Shocks are seen to form at the interface between slow-moving fluid in the δ-scale bulges of the redeveloping boundary layer and the high-speed

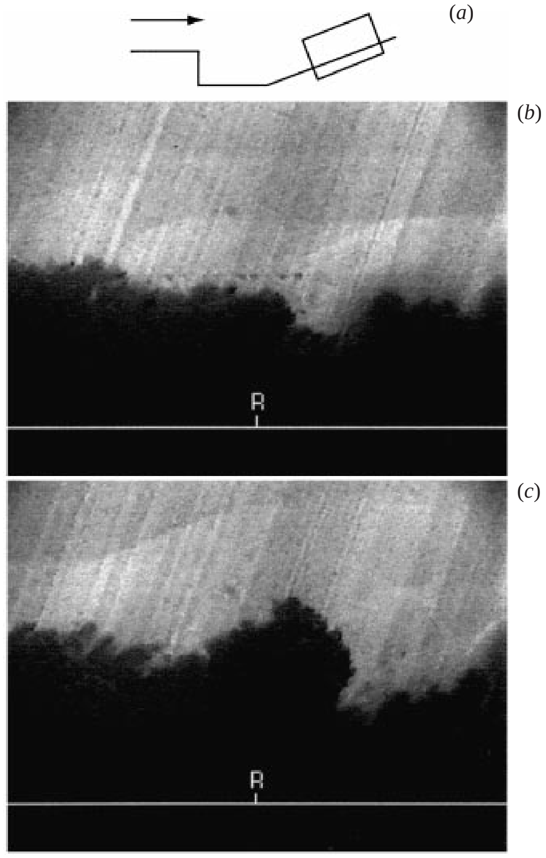

FIGURE 5. Side-view laser scattering images of flow along reattachment ramp. (*a*) Experimental configuration, not to scale. (*b*) Undisturbed flow. (*c*) Air injection through three holes.

fluid of the free stream. These shocks are relatively weak, and are made visible by an increase in the intensity of scattered light due to the increased density of scattering particles downstream of the shocks. Shocks are associated with organized structures having a wide range of length scales, and the strongest shocks are associated with structures with scales on the order of the thickness of the redeveloping boundary layer ($\delta_r = 10.4\,\mathrm{mm}$).

Images obtained in this region of the flow are quite similar to those obtained by Smith & Dutton (1996) near the mean 'reattachment' point of a planar base flow. This similarity is not surprising considering that the wall shear stress is very low near mean reattachment in the present flow, and the presence of the no-slip wall does not significantly affect the shear layer until farther downstream (see Settles *et al.* 1982). The flow turning, and consequent compression, are the main reason for the relatively strong shocks that appear on the upstream sides of the large-scale structures in the reattachment region of the two flows.

Figure 5(*c*) shows a typical example image for the case with air injection through one hole in the cavity of the experimental model. There is a dramatic increase in the thickness of the redeveloping boundary layer, the scale of the turbulence structures, and the strength of the shock waves. (The change in length scale will be quantified in figure 7.) Again, there is an association of shocks with large-scale structures in the shear layer.

For plan views of the reattaching flow, a horizontal laser sheet generated with the Spectra Physics ArF laser was positioned 38 mm off the floor of the cavity in the experimental model. The field of view was 31 mm from top to bottom, and began 121 mm downstream of the backward-facing step (see figure 6*a*). The flow direction is from top to bottom in the images, with a component that passes up through the laser sheet from below. For these images the laser sheet is relatively far from the wall, where the compression due to the 20° turning angle occurs over a relatively short streamwise distance. Consequently, stronger shocks tend to vaporize the scattering particles here, and in the images the flow appears dark downstream of these shocks.

The flow over this portion of the experimental model is highly complex and unsteady, even in the absence of air injection (figure 6*b*). The shock system exhibits spanwise wrinkling with a length scale on the order of the reattachment boundary layer thickness. Note the bowed white line in the figure, representing a plan-view section of a shock associated with an organized structure, and the darker region downstream, reflecting the vaporization of the scattering particles by the primary oblique shock. Additional examples of this spanwise wrinkling may be found in Poggie (1995) and in Shen *et al.* (1993).

An image of the flow with air injection through the centre hole downstream of the backward-facing step is shown in figure 6(*c*). In this image, a bow shock is clearly seen associated with the upstream side of a structure in the redeveloping boundary layer.

In order to quantify the increase in the length scale of the coherent structures seen in the images, two-point cross-correlations were carried out for the set of side-view images of the reattachment region (see figure 5). The cross-correlation between the scattering intensity at a reference point $I(X,Y)$ and the scattering intensity at a given point in the field of view $I(x,y)$ was defined as

$$R_I(x,y,X,Y) = \frac{\mathrm{Cov}[I(x,y), I(X,Y)]}{\{\mathrm{Var}[I(x,y)]\mathrm{Var}[I(X,Y)]\}^{1/2}}, \tag{3.1}$$

where the variance and covariance are defined in the usual way, that is

$$\mathrm{Var}(I) = \sum_{i=1}^{N} (I_i - \bar{I})^2/N, \tag{3.2}$$

and

$$\mathrm{Cov}(I,J) = \sum_{i=1}^{N} (I_i - \bar{I})(J_i - \bar{J})/N. \tag{3.3}$$

Here N is the number of images, and an overbar indicates an average over the set of images. This type of correlation is similar to the zero-time-delay cross-correlation between a pair of point probes for different probe separations.

The horizontal position of the reference point was taken to be $X = 60.5$ mm, where X is the distance along the reattachment ramp. In order to allow a consistent comparison between the two cases, the vertical coordinate was taken to be the location of maximum root-mean-square scattering intensity (about $Y = 6$ mm for the undisturbed flow and $Y = 10$ mm for the case with air injection, where Y is the normal distance from the surface of the reattachment ramp).

The results are shown in figure 7. Contours are shown from 0.4 to 0.9, with an interval of 0.1. The correlation contours generally have an elliptical shape, as seen in other studies of free shear layers and boundary layers (see Smith 1989; Smith & Dutton 1996). One feature of note, however, is the apparent horizontal orientation

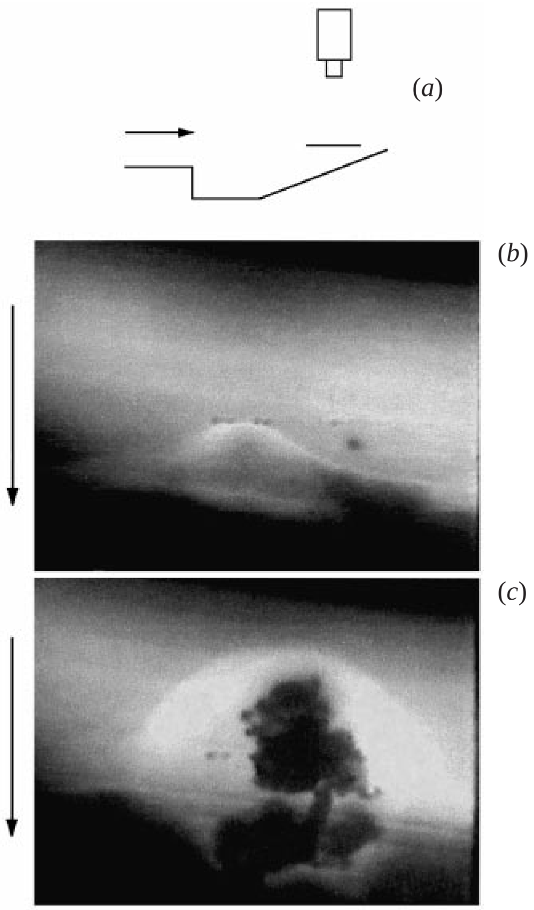

FIGURE 6. Horizontal section through reattachment shock system. Field of view aligned with model centreline; mean flow direction downward and out of the page. (*a*) Experimental configuration, not to scale. (*b*) Undisturbed flow. (*c*) Air injection through one hole.

of the contours. This apparent orientation occurs because the field of view for these images is aligned with the reattachment ramp (see figure 5*a*). The structures are actually inclined about 20° from the local mean flow direction at the reference point.

The primary difference between the baseline case and the perturbed flow is a dramatic increase in the length scale of the coherent structures. For example, the horizontal length scale δ_c of the $R_I = 0.5$ contour increases from about $\delta_c = 6\,\mathrm{mm}$ for the undisturbed flow to about $\delta_c = 9\,\mathrm{mm}$ for the case with air injection. For comparison, the boundary layer thickness near the mean reattachment line in the undisturbed flow is $\delta_r = 10.4\,\mathrm{mm}$.

3.3. *Double-pulse laser scattering*

Double-pulse laser scattering experiments were carried out using a vertical laser sheet to obtain side views of the flow over the ramp. For these experiments, the field of view was aligned with the floor of the cavity in the experimental model rather than with the reattachment ramp. The field of view was 58 mm wide by 43 mm high, and began 92 mm downstream of the backward-facing step. The bottom edge of the field of view lay 14 mm above the cavity floor.

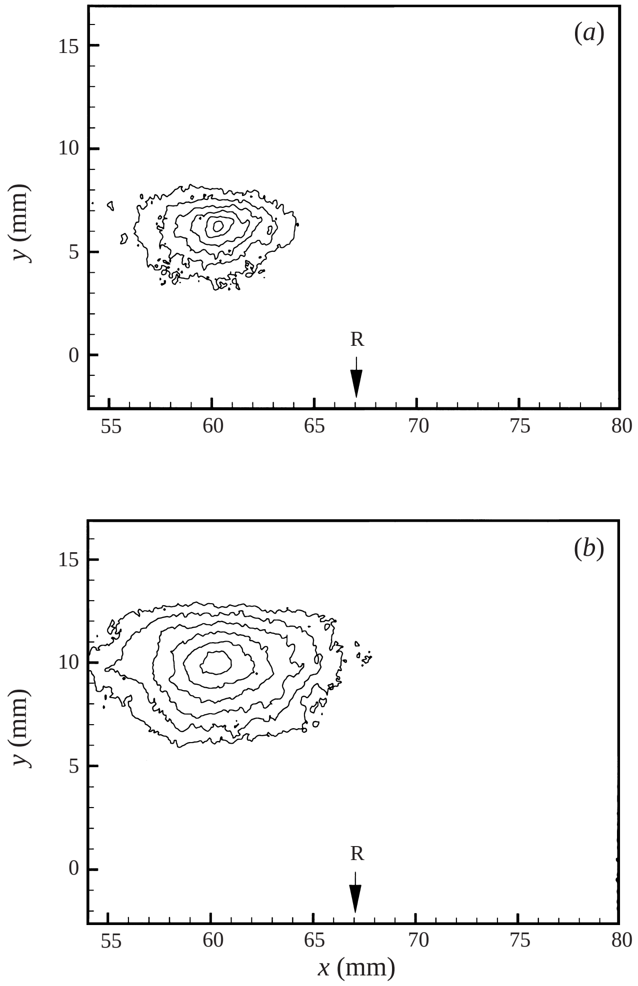

FIGURE 7. Two-point auto-correlation of side-view images. (*a*) Undisturbed flow, $N = 340$. (*b*) Air injection, $N = 236$.

Camera alignment and magnification were carefully checked to avoid introducing an illusion of motion in the images. To illustrate that these properties were accurately matched, figure 8 shows a pair of example images of the undisturbed flow for the case with zero time delay (single-pulse mode). Note that the images have been processed to reduce the effects of laser sheet non-uniformity. The mean reattachment location for the undisturbed flow is marked 'R' in the figure, and the ramp surface is indicated with a line. Both large-scale turbulence structures and the reattachment shock system are visible in the images, and the fields of view are seen to be closely aligned. The free shear layer enters the field of view from the lower left side of each image, and reattaches on the 20° ramp, forming a new boundary layer which exits near the upper right of the images. The great variability of the thickness of the turbulent boundary layer visible in the reattachment region is consistent with the high degree of intermittency found by Hayakawa *et al.* (1984) in hot-wire data obtained in this region of the undisturbed flow. As in the images shown above, shocks are seen to form at the upstream sides of the bulges in the redeveloping boundary layer.

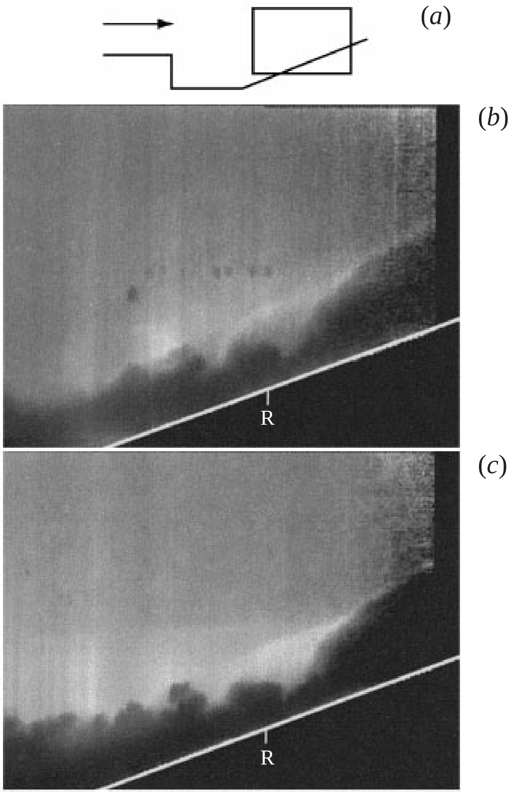

Figure 8. A pair of images of the undisturbed flow taken with the dual-camera configuration and the laser in single-pulse mode. (*a*) Field of view, not to scale. (*b*) Camera One. (*c*) Camera Two.

Figure 9 shows a pair of images of the undisturbed flow taken with a time delay of 30.2 μs. The top image was captured with one video camera, and the bottom image was captured after the time delay with the other camera. This pair of images was selected because it shows a particularly large structure entering the reattachment zone, where a relatively strong shock forms on its upstream side. Note that a shock associated with the upstream edge of the structure appears to convect along with it as the structure moves downstream.

Convection velocities, derived from fluctuating pressure measurements on the ramp, initially have a relatively high value of $\sim 0.9U_e$, which is characteristic of the free shear layer, and decrease along the ramp to values ($\sim 0.7U_e$) more characteristic of a turbulent boundary layer at the present Mach number (see figure 14 and Poggie 1995). Convection velocities of $\sim 0.8U_e$, derived from the present images, agree with the pressure fluctuation data measured near the mean reattachment point, 'R'.

A similar set of images was obtained in the flow perturbed by air injection through the centre hole in the cavity of the experimental model. A pair of images showing a structure entering the reattachment zone is shown in figure 10. Although the length scale of the structures is much larger in the disturbed flow, the qualitative behaviour of the structures is similar to that seen in the undisturbed flow: a shock is present on the upstream edge of a given structure, and moves with the structure as it convects downstream along the ramp. Convection velocities derived from the images for this case show an increase over the undisturbed flow case; this change will be quantified in figure 14.

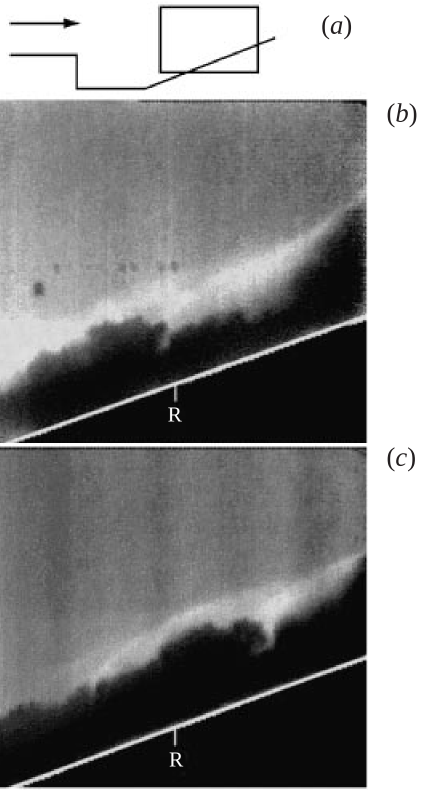

FIGURE 9. A pair of double-pulse images obtained in the undisturbed flow using a delay of 30.2 μs. (*a*) Field of view, not to scale. (*b*) Camera One. (*c*) Camera Two.

3.4. *Pressure measurements*

Measurements of the mean and fluctuating surface pressure were made along the reattachment ramp for the undisturbed flow and for the case with air injection through three holes in the cavity of the experimental model. Figure 11(*a*) shows the results for the mean pressure, which are normalized by the static pressure in the free-stream flow, p_{ref}. The pressure is seen to rise monotonically from the free-stream level to the level downstream of the primary oblique shock. With air injection, the pressure rise begins slightly sooner, but the pressure increases more slowly along the streamwise direction, and reaches approximately the same level downstream.

The pressure distributions were found to collapse onto one curve when plotted against the non-dimensional distance $(x - x_r)/\delta_c$, where the mean reattachment location was taken to be $x_r = 67\,\mathrm{mm}$ (based on flow visualization) for the undisturbed flow and $x_r = 75\,\mathrm{mm}$ (picked to collapse the data) for the case with air injection (figure 11*b*). The following equation was found to provide a good fit to the reduced data:

$$\frac{p}{p_{\mathrm{ref}}} = \frac{11}{4} + \frac{7}{4}\mathrm{erf}\left(\frac{x - x_r}{4\delta_c} + 0.1\right). \tag{3.4}$$

These results indicate that the broader pressure distribution observed with air injection reflects primarily the increase in the thickness of the reattaching shear layer, rather than (for example) a large-scale shear layer flapping motion.

Figure 12 shows the standard deviation of the wall pressure fluctuations $\sigma_p = (\overline{p'^2})^{1/2}$

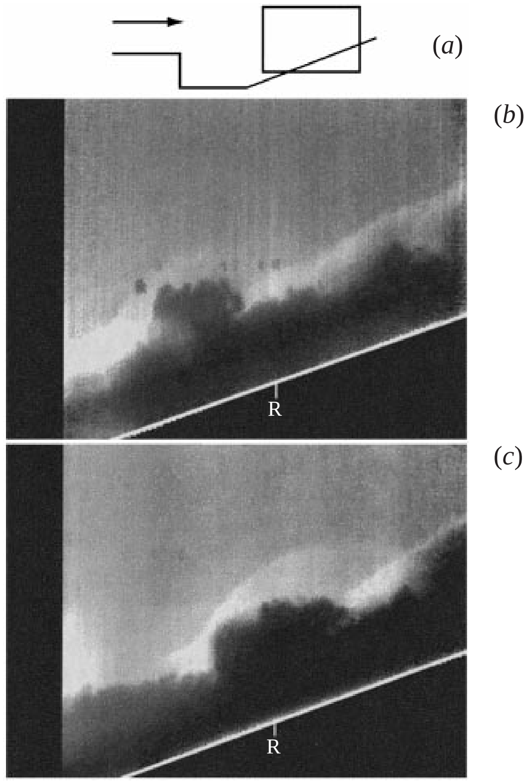

Figure 10. A pair of double-pulse images obtained in the flow with air injection through one hole using a delay of 30.2 μs. (*a*) Field of view, not to scale. (*b*) Camera One. (*c*) Camera Two.

in the undisturbed flow plotted versus position along the ramp. The measurements of Shen *et al.* (1993), for the same geometry and flow conditions, are shown for comparison. The data have been normalized by the static pressure p_{ref} in the free-stream flow. An uncertainty bar of $\pm 0.05 p_{\text{ref}}$ indicates the level of scatter in the data. The intensity of the pressure fluctuations in the present flow is somewhat higher than that found by Shen *et al.*, primarily because of the removal of the aerodynamic fences and sidewall inserts to allow optical access to the flow (Poggie 1995). Nevertheless, both data sets show a rise in the pressure fluctuation levels to a peak downstream of the mean reattachment line, followed by a gradual decrease downstream.

Figure 13(*a*) compares the pressure fluctuation levels in the undisturbed flow to the case with air injection into the flow through three holes on the cavity centreline. The distribution of the intensity of the pressure fluctuations has the same shape in the air injection case as in the undisturbed flow case, but is shifted upward significantly. There is an increase of about 50% in the standard deviation of the pressure signal at the station farthest upstream. Given that the pressure fluctuations are caused primarily by shock motion, this change is consistent with the apparent increase in the amplitude of the shock motion observed in the flow visualization data, and indicates a strong connection between the incoming disturbances and the shock motion in the flow.

Plotkin's model gives an estimate of the intensity of the pressure fluctuations (1.6), provided that the streamwise component of the mean pressure gradient and the amplitude of the shock motion are known. Here we take the correlation length

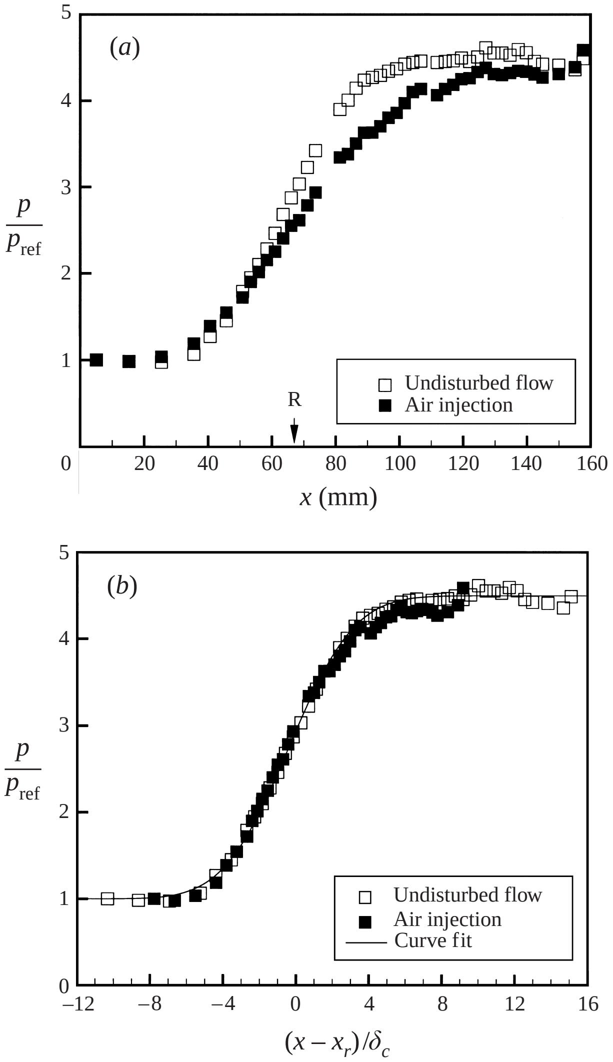

FIGURE 11. Mean wall pressure distribution along ramp. (*a*) Dimensional distance. Mean reattachment location marked as 'R'. (*b*) Non-dimensional distance.

scale as a measure of the amplitude of the shock motion: $\overline{x^2} \approx \delta_c^2$, and use the derivative of (3.4) to determine the streamwise pressure gradient. The results of using these quantities in (1.6) are shown in figure 13(*b*), plotted against the non-dimensional streamwise position. Since the mean pressure distribution collapsed in non-dimensional coordinates for the undisturbed flow and air injection cases, its derivative $\partial\bar{p}/\partial x$ also does, and the theory predicts the single curve shown in the figure. The theory gives the correct order of magnitude for the location and value of the peak pressure fluctuation intensity, but does not predict the increase in intensity observed with air injection.

Cross-correlation calculations were made between adjacent pairs of pressure transducers. Figure 14 shows an example cross-correlation plot for a pair of transducers located 82.6 and 87.6 mm up the ramp. This location was chosen because it lies near the point of maximum intensity in the wall pressure fluctuations. The single peak in

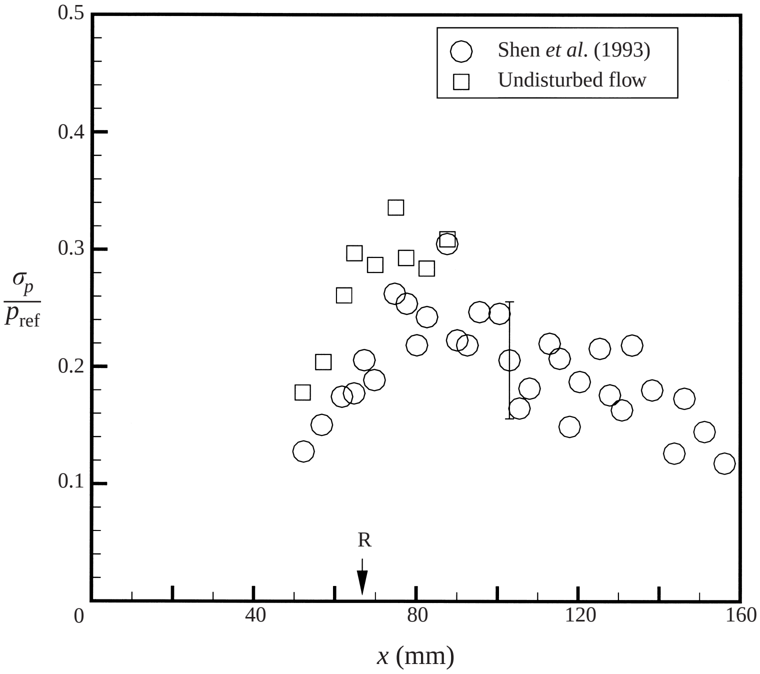

FIGURE 12. Intensity of wall pressure fluctuations along ramp. Mean reattachment location marked as 'R'.

the cross-correlation indicates the downstream convection of the large-scale structures in the redeveloping boundary layer. The effect of air injection was to increase the peak correlation, increase the speed of the structures (reduce the optimum time delay), and increase the width of the correlation function. With air injection, the convection velocity (adjusted to a nominal stagnation temperature of 270 K) increased from $U_c = 478\,\mathrm{m\,s^{-1}}$ to $U_c = 577\,\mathrm{m\,s^{-1}}$. (For comparison, the boundary edge velocity near mean reattachment is about $572\,\mathrm{m\,s^{-1}}$ for $T_0 = 270\,\mathrm{K}$.) A similar change is evident in convection velocities derived from the flow visualization data set corresponding to figures 9 and 10.

An important parameter identified by Plotkin (1975) in setting the characteristic frequency of the power spectrum is the integral time scale of the auto-correlation (1.3). Auto-correlations for the transducer located at $x = 82.6\,\mathrm{mm}$ are shown in figure 15. A significant increase in the characteristic time scale of the auto-correlation is seen with air injection: the integral time scale increases from about 35.4 μs to 44.5 μs. The non-dimensional time scale, however, remains approximately constant, changing from $\tau_p U_c/\delta_c = 2.73$ for the undisturbed flow to 2.79 with air injection.

(We note, as an aside, that the auto-correlations shown in figure 15 have relatively long tails. To ensure that the integral time scale was evaluated correctly, we plotted the quantity $\int_0^T R_p(\tau)\,\mathrm{d}\tau$ vs. T, and stopped the integration where the integral converged to a constant value. For the present data, we found a fairly unambiguous plateau near $T = 1.3\,\mathrm{ms}$.)

Figure 16 shows the corresponding auto-spectra of the fluctuating pressure signal. The data are seen to have a broad-band energy content, with no prominent peaks. The roll-off at higher frequency is a property of the flow, not the signal processing system: the fourth-order Butterworth filter passes about 70% of the input amplitude

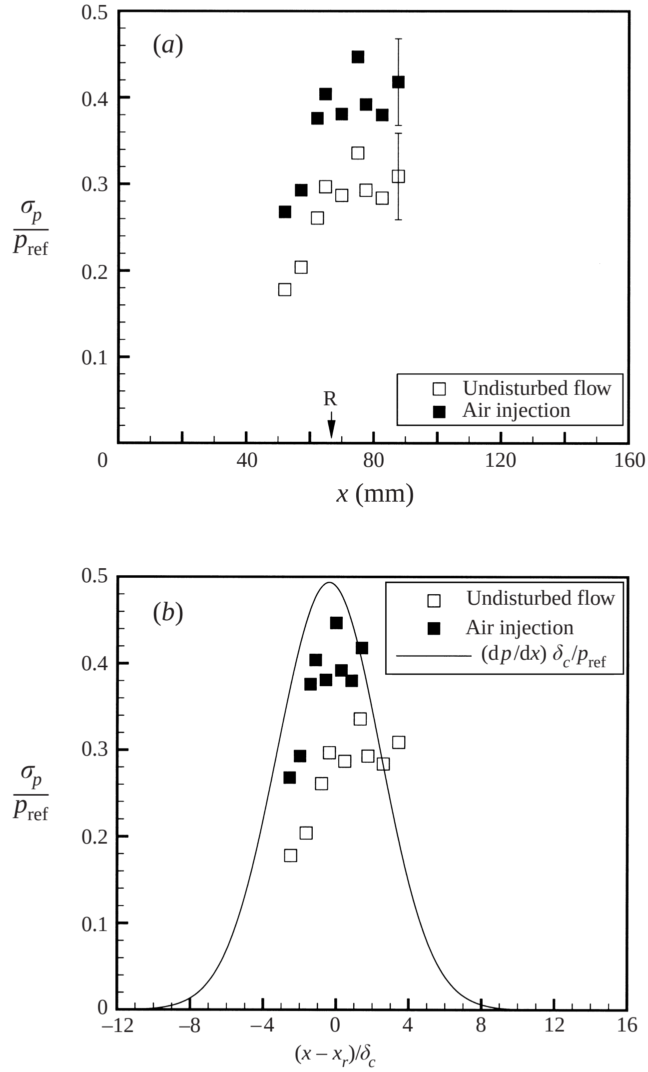

FIGURE 13. Effect of air injection on wall pressure fluctuations. (*a*) Dimensional distance. Mean reattachment location marked as 'R'. (*b*) Non-dimensional distance.

at the cut-off frequency of 80 kHz. Air injection is seen to shift the spectrum up, reflecting the increase in the intensity of pressure fluctuations. Analogous features in the spectra are also seen to be shifted left in the air injection case, reflecting a decrease in characteristic frequency. Note, in particular, the leftward shift in the 'knee' in the spectrum, which is present near 2 kHz in the undisturbed flow data.

Figure 17(*a*) shows the spectral data plotted in normalized form. The frequency was non-dimensionalized by the correlation length scale δ_c and the convection velocity U_c. The spectrum was divided by the mean-square fluctuating pressure $\overline{p'^2}$ and the time scale δ_c/U_c. The data collapse well. In particular, non-dimensionalizing the frequency causes the 'knees' in the spectra to line up.

The non-dimensionalization also leads to good collapse of the auto-correlations, as shown in figure 17(*b*). (Compare with figure 15.) Particularly good collapse is obtained

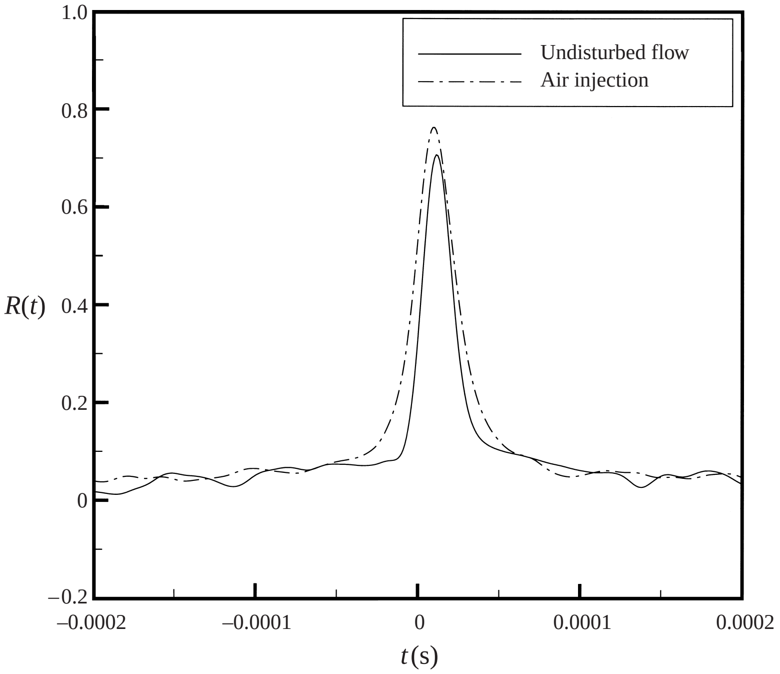

FIGURE 14. Cross-correlations of pressure signals at $x = 82.6\,\text{mm}$ with $\Delta x = 5.1\,\text{mm}$. Sampling rate 1 MHz, window size 2048 points.

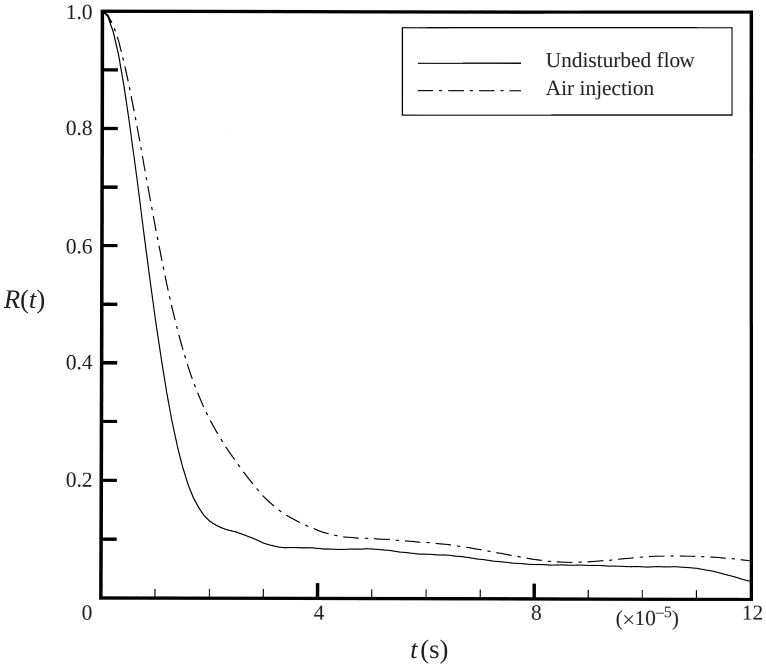

FIGURE 15. Auto-correlations of pressure signals at $x = 82.6\,\text{mm}$. Sampling rate 1 MHz, window size 2048 points.

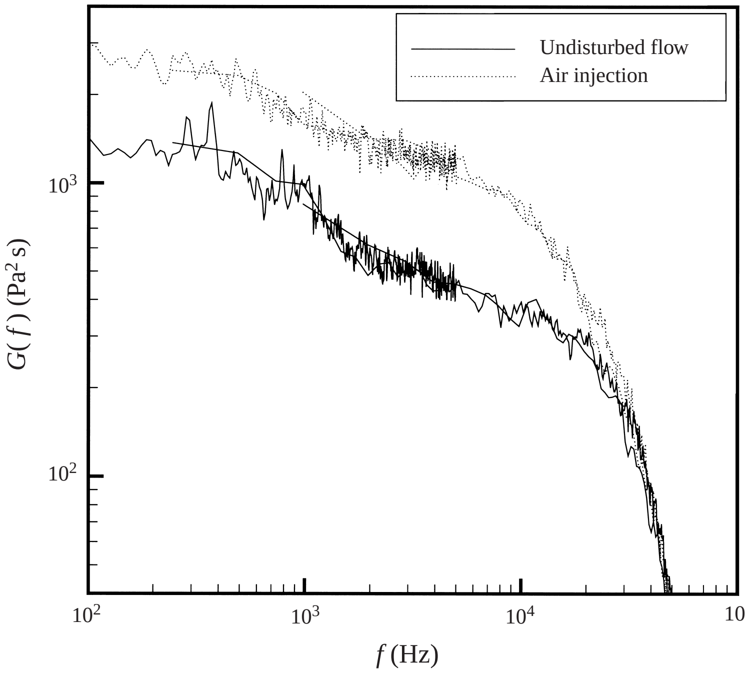

FIGURE 16. Auto-spectra for the wall pressure fluctuation data at $x = 82.6$ mm. Sampling rates 10 kHz, 250 kHz, and 1 MHz; window size 1024 points.

for short time delays, $U_c t/\delta_c < 1$, and for the long tails of the correlations, $U_c t/\delta_c > 3$. These results are consistent with the observation that the non-dimensional integral time scale stays approximately constant at $\tau_p U_c/\delta_c \approx 2.7$.

4. Comparison with theoretical model

Before making a detailed comparison of Plotkin's model to the reattaching shear layer data, we will briefly compare the model to data obtained in a blunt fin flow, which was examined previously by Poggie & Smits (1997). We include this digression because the theoretical model has not, to the best of our knowledge, been compared to any experimental data since Plotkin's original paper. The reattaching shear layer flow is a special flow in the sense that the separation point is essentially fixed at the backward-facing step, so it is worth briefly examining how Plotkin's model fits a more conventional separated turbulent flow.

The experimental model used by Poggie & Smits (1997) was an unswept fin mounted normal to the wind tunnel floor at zero angle of attack. The leading edge was a semi-circular cylinder of diameter $D = 19$ mm, and the free-stream conditions were essentially the same as those described here for the reattaching shear layer flow. The incoming turbulent boundary layer flow was the one studied by Spina & Smits (1987); the boundary layer thickness just upstream of the interaction was $\delta_0 = 28$ mm.

A horseshoe vortex system and its associated λ-shock system are the dominant features of the three-dimensional, separated flow near the juncture of the fin and the plate. The blunt fin flow is typical of the class of flows described in the Introduction in that the legs of the λ-shock system move with the expansion and contraction of the separation bubble to produce intense fluctuations in pressure and heat flux ahead

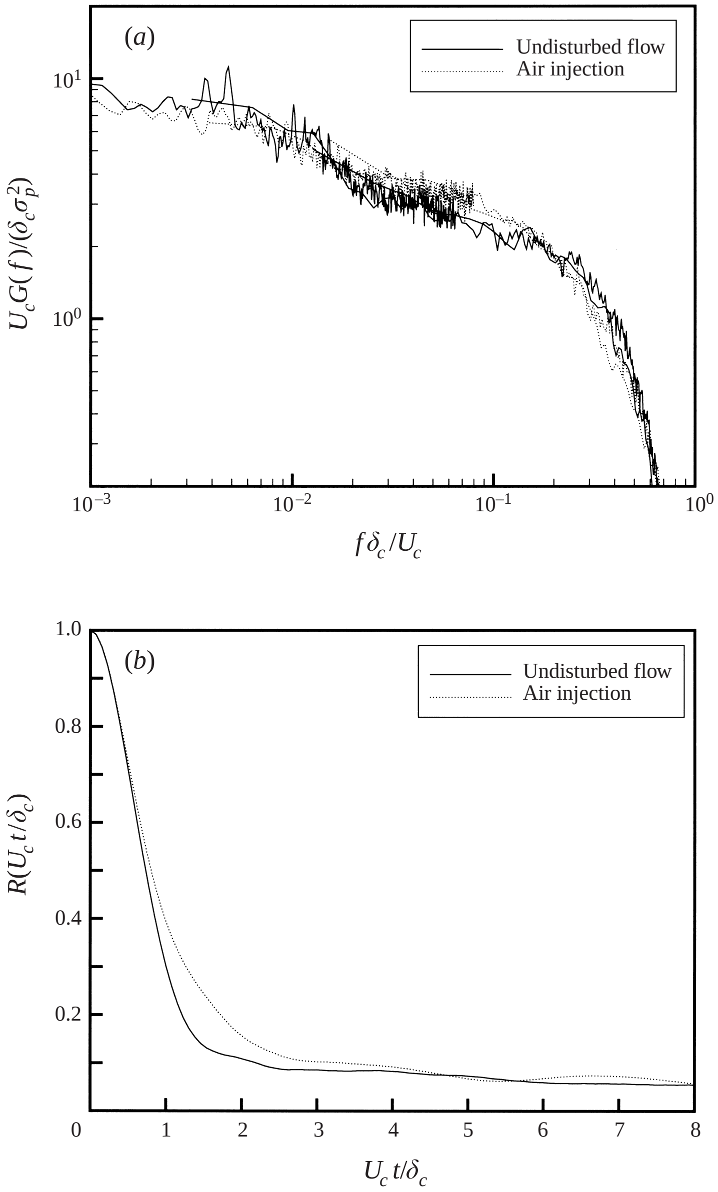

FIGURE 17. Non-dimensionalized wall pressure fluctuation data at $x = 82.6$ mm. (*a*) Auto-spectrum. (*b*) Auto-correlation.

of the fin. Here we examine measurements of the wall pressure fluctuations made at $x/D = -2.4$ and $x/D = -1.27$, which correspond to regions of unsteady separation and reattachment, respectively. (Here x is the distance along the flow centreline, with negative values measured upstream from the fin root.)

The results for the upstream station, where the integral time scale is $\tau_p = 281.4\,\mu$s, are shown in figure 18. (Here the integration of the auto-correlation to obtain τ_p was carried out to 1.62 ms, where the integral converged to an essentially constant value.) The spectrum predicted by (1.7) is seen to be an excellent fit to the experimental data over more than two decades of normalized frequency, figure 18(*a*), with a departure

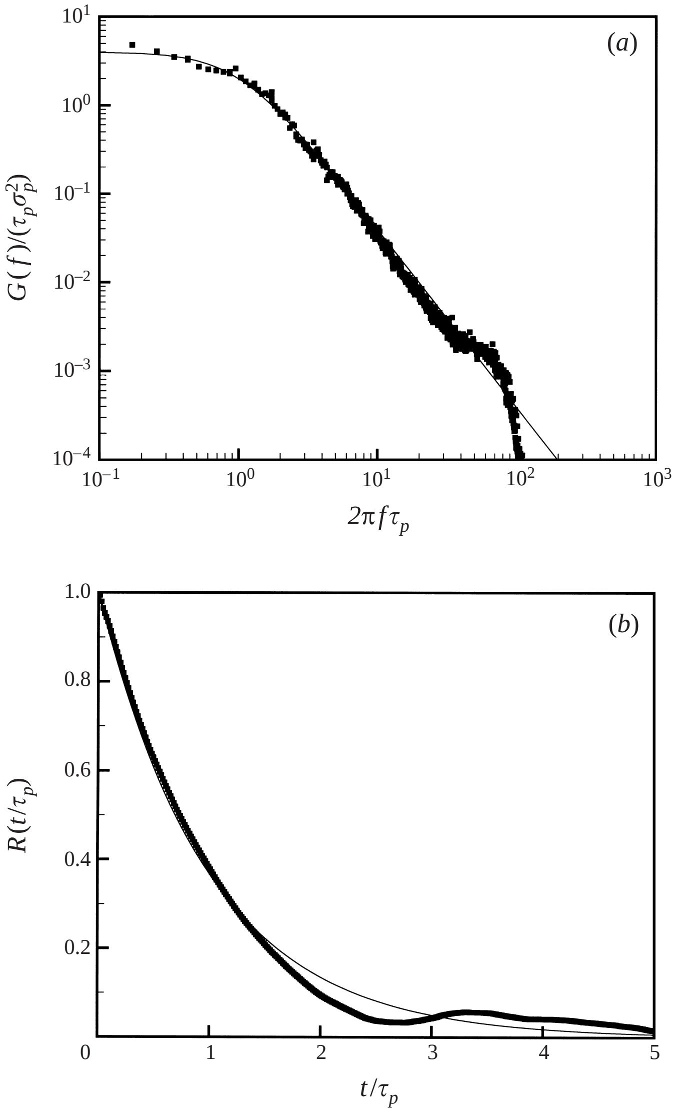

FIGURE 18. Blunt fin data at $x/D = -2.4$ fit to theoretical model. (*a*) Spectra. Sampling rates 50 kHz, 250 kHz, and 1 MHz; window size 1024 points. (*b*) Auto-correlation. Sampling rate 250 kHz; window size 2048 points.

from the model at $2\pi f \tau_p \approx 50$. The auto-correlation predicted by (1.5) is seen in figure 18(*b*) to also be a reasonably good fit to the experimental data. This good agreement indicates that, through the long time scale introduced by the parameter τ_R (equivalently τ_p), the model is able to mimic the manner in which the relatively broad-band forcing by the turbulent velocity fluctuations in the incoming flow can lead to relatively low-frequency motion of the shock system.

If we define a characteristic frequency $f_p = 1/(2\pi\tau_p)$, and compute a non-dimensional frequency, we find $f_p L_i / U_\infty \approx 0.02$, where $L_i \approx 0.8D$ is the length of the region of intermittent separation shock motion. This result is in good agreement with the scaling of the maximum shock crossing frequency found by Gonsalez & Dolling (1993) for a variety of separated turbulent flows.

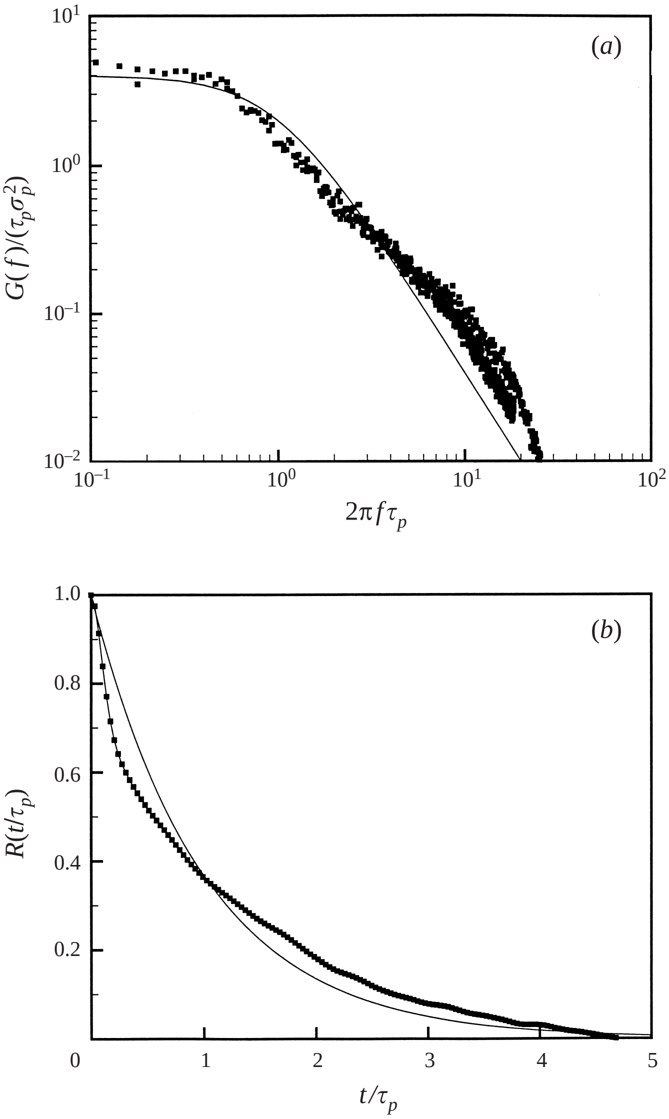

FIGURE 19. Blunt fin data at $x/D = -1.27$ fit to theoretical model. (*a*) Spectra. Sampling rates 50 kHz, 250 kHz, and 1 MHz; window size 1024 points. (*b*) Auto-correlation. Sampling rate 250 kHz; window size 2048 points.

The spectrum measured at the downstream ($x/D = -1.27$) station, where $\tau_p = 117.0\,\mu s$ (integration carried out to 0.55 ms), also shows fairly good agreement with the model, but over a more limited range, figure 19(*a*). (Note the different ranges on the axes of this plot compared to figure 18.) Here the departure from the model begins at $2\pi f\tau_p \approx 2$, and the theoretical curve is somewhat shifted away from the data. A similar trend is seen in the auto-correlation results shown in figure 19(*b*). The relatively poorer fit here may be due to an overlap in the frequency ranges of the large-scale shock motion and the flow turbulence in this part of the flow. The assumption that the shock response is much slower than the turbulent fluctuations ($\tau_R \gg \tau_u$) would then be a poorer approximation.

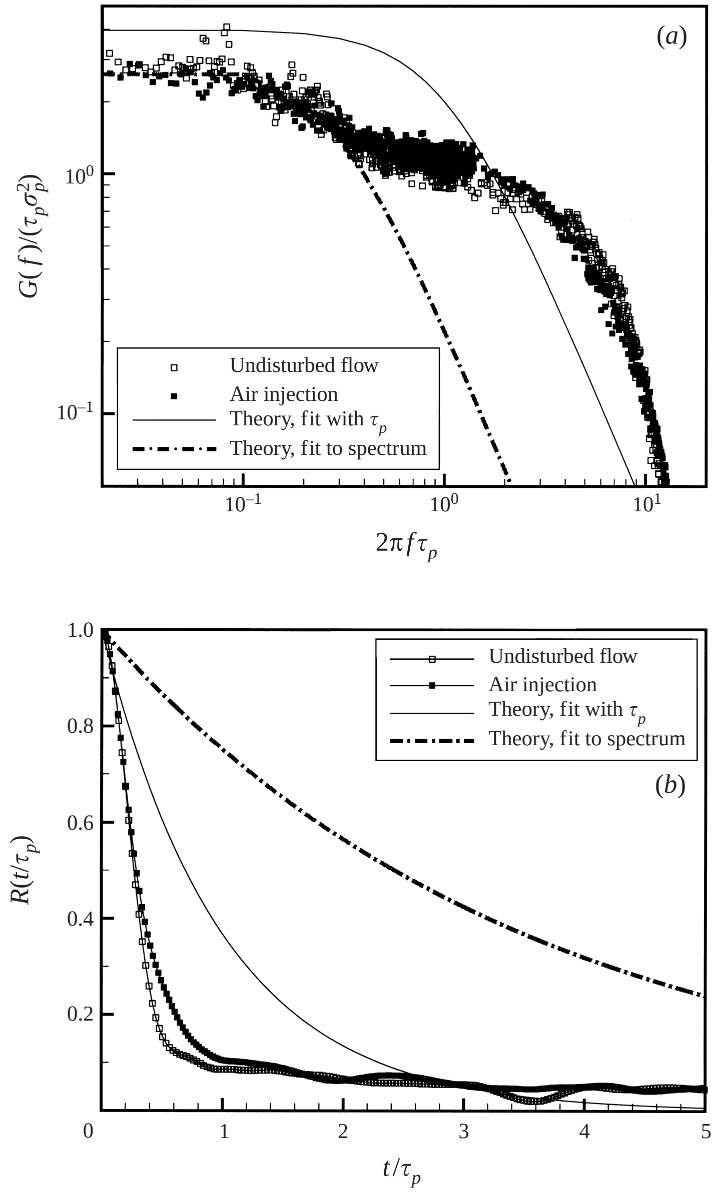

FIGURE 20. Wall pressure fluctuation data at $x = 82.6$ mm compared to Plotkin's theory. (*a*) Auto-spectrum. (*b*) Auto-correlation.

We return to the reattaching shear layer flow in figure 20. The open and closed symbols represent the undisturbed flow and air injection cases, respectively. In each case, the data are normalized by the corresponding mean-square fluctuating pressure and integral time scale. (As discussed previously, the time scales are $\tau_p = 35.4\,\mu\text{s}$ for the undisturbed flow, and $44.5\,\mu\text{s}$ for the case with air injection.) As expected from the results shown in figure 17, and the fact that the non-dimensional integral time scale is essentially the same for the two cases, the air injection and undisturbed flow data collapse nicely when plotted in this form.

The solid lines indicate the theory. The agreement between the theoretical model and the data is relatively poor compared to that obtained for the blunt fin flow. Interestingly, the data depart from the model in a manner similar to that seen for the blunt fin flow. For relatively low frequencies, and large time scales, the data behave in a manner similar to the model. In particular, the theoretical spectrum can be made to closely fit the range $2\pi f \tau_p < 0.4$ for the shear layer data by introducing adjustable parameters $\hat{\sigma}_p$ and $\hat{\tau}_p$ in the theory. This is shown as a dash-dot line in figure 20(*a*). (Note that the values of $\hat{\sigma}_p$ and $\hat{\tau}_p$ used to calculate this line are different from the values of σ_p and τ_p used to non-dimensionalize the axes of the plot.) For relatively higher frequencies, the data depart from the form of the model. In contrast to the blunt fin flow, most of the energy in the spectrum is concentrated in these high-frequency motions, which are related to direct perturbation of the shock by the incoming flow turbulence.

5. Conclusions

The origin of shock unsteadiness in a Mach 2.9 turbulent, reattaching shear layer was investigated experimentally using temporally resolved flow visualization and measurements of wall pressure fluctuations. In this flow, the separation point is essentially fixed at a backward-facing step, and the reattachment point is free to move along a ramp.

In order to investigate the influence of disturbances originating in the incoming shear layer, experiments were conducted in which artificial disturbances were introduced into the flow through steady air injection in the vicinity of separation. The effect on the reattachment shock system was dramatic: the intensity of the pressure fluctuations and the amplitude of the shock motion increased substantially, and power spectra of the pressure fluctuations showed a distinct shift to lower frequency. Mean pressure profiles on the reattachment ramp collapsed onto a common curve in non-dimensional coordinates based on a length scale derived from two-point cross-correlations of the flow visualization data. Similarly, the power spectra of the pressure fluctuations collapsed in coordinates based on this same length scale and a convection velocity derived from cross-correlations of the pressure measurements.

The data were compared to a theory developed by Plotkin (1975), which is based on perturbation of a shock by random fluctuations in the incoming turbulent flow. Plotkin's model mimics the manner in which relatively broad-band perturbations in the incoming turbulent flow can lead to relatively low-frequency motion of the separation bubble and its associated shock system. A relatively long time scale, characteristic of the separation bubble flow, enters the model through the restoring time scale τ_R.

Where the shock motion is dominated by the low-frequency component, characterized by τ_R, an excellent fit is obtained to the data. This is the case for the upstream station in the blunt fin flow discussed briefly above. The fit becomes poorer when the shock motion contains significant contributions at higher frequencies due to direct perturbations by the incoming turbulent structures, characterized by $u(t)$ in the model. This seems to be the case for reattachment shock motion, as in the downstream station in the blunt fin flow and in the reattaching shear layer flow. The low-frequency motion is detectable in the spectra near reattachment, but contains less energy relative to the shock motions caused by direct perturbations by the incoming turbulent structures. We note, however, that the functional relationship $G(f)/(\overline{p'^2}\tau_p) = \mathrm{func}(2\pi \mathrm{f} \tau_\mathrm{p})$ still seems to hold in these cases, and data from the undisturbed and perturbed reattaching shear layer flows collapse in this form.

The assumptions used by Plotkin to obtain analytical expressions for the auto-correlation and auto-spectrum limit the applicability of these expressions to the low-frequency, long-time-scale component of the shock motion. Discrepancies between the model and the data for reattachment shock oscillation may thus reflect the assumptions used to derive (1.5) and (1.7), rather than the model ordinary differential equation (1.1). Indeed, spectra derived from numerical solutions of (1.1) for random input signals show a deviation at high frequency from (1.7) in much the same manner as the experimental data. We hope to present these results in a future paper.

In summary, the results indicate that the shock motion in the reattaching shear layer is primarily caused by organized structures in the incoming turbulent flow. Direct evidence for this conclusion was obtained in the flow visualization experiments, where shocks were observed to form on the upstream sides of large-scale organized structures as they convected through the reattachment region. Further evidence was provided by the collapse of the spectra of the wall pressure fluctuations, which are caused primarily by shock motion, in non-dimensional coordinates based on the convection velocity and length scale of these structures. Finally, the fluctuating pressure spectra display relatively little energy content in the low-frequency mode that is characteristic of conventional separated boundary layer flows, such as the blunt fin flow.

This research was funded in part by grants from the Air Force Office of Scientific Research and the National Aeronautics and Space Administration Langley Research Center. J. Poggie received support from a National Science Foundation Graduate Research Fellowship and the United States Air Force PALACE KNIGHT program during the course of this research program.

R. Bogart and W. Stokes provided technical support for this project. The Princeton University laser physics group, and in particular Dr J. Forkey and Professor R. B. Miles, provided assistance in the laser visualization experiments. The first author would like to thank Dr A. E. S. Creese, Dr R. L. Kimmel, and Dr J. D. Schmisseur for advice in the preparation of this paper.

REFERENCES

Baca, B. K. 1981 An experimental study of the reattachment of a free shear layer in compressible turbulent flow. Master's thesis, Princeton University, Princeton, NJ.

Bogar, T. J. 1986 Structure of self-excited oscillations in transonic diffuser flows. *AIAA J.* **24**, 54–61.

Brusniak, L. & Dolling, D. S. 1994 Physics of unsteady blunt-fin-induced shock wave/turbulent boundary layer interactions. *J. Fluid Mech.* **273**, 375–409.

Brusniak, L. & Dolling, D. S. 1996 Engineering estimation of fluctuating loads in shock wave/turbulent boundary-layer interactions. *AIAA J.* **34**, 2554–2561.

Cogne, S., Forkey, J., Lempert, W., Miles, R. B. & Smits, A. J. 1993 Evolution of large-scale structures in a supersonic turbulent boundary layer. In *Transitional and Turbulent Compressible Flows*. ASME FED, vol. 151 (ed. L. D. Kral & T. A. Zang), pp. 229–237.

Dolling, D. S. 1993 Unsteady phenomena in shock wave/boundary layer interaction. In *Special Course on Shock-Wave/Boundary-Layer Interactions in Supersonic and Hypersonic Flows*, AGARD R-792 (ed. G. Degrez), pp. 4-1–4-46. NATO Advisory Group for Aerospace Research and Development, Neuilly Sur Seine, France.

Dolling, D. S. 1998 High-speed turbulent separated flows: Consistency of mathematical models and flow physics. *AIAA J.* **36**, 725–732.

Dolling, D. S. & Murphy, M. T. 1983 Unsteadiness of the separation shock wave structure in a supersonic compression ramp flowfield. *AIAA J.* **21**, 1628–1634.

Driver, D. M., Seegmiller, H. L. & Marvin, J. G. 1987 Time-dependent behavior of a reattaching shear layer. *AIAA J.* **25**, 914–919.

Eaton, J. K. & Johnston, J. P. 1982 Low frequency unsteadiness of a reattaching turbulent shear layer. In *Turbulent Shear Flows 3* (ed. L. J. S. Bradbury, F. Durst, B. E. Launder, F. W. Schmidt & J. H. Whitelaw), pp. 162–170. Springer.

Erengil, M. E. & Dolling, D. S. 1991 Correlation of separation shock motion with pressure fluctuations in the incoming boundary layer. *AIAA J.* **29**, 1868–1877.

Erengil, M. E. & Dolling, D. S. 1993 Physical causes of separation shock unsteadiness in shock wave/turbulent boundary layer interactions. *AIAA Paper* 93-3134.

Erlebacher, G & Hussaini, M. Y. 2000 Shock-shape alteration caused by interaction with organized strucures. *AIAA J.* **38**, 1002–1009.

Forkey, J., Cogne, S., Smits, A. & Bogdonoff, S. 1993 Time-sequenced and spectrally-filtered imaging of shock wave and boundary layer structure for inlet characterization. *AIAA Paper* 93-2300.

Gonsalez, J. C. & Dolling, D. S. 1993 Correlation of interaction sweepback effects on the dynamics of shock-induced turbulent separation. *AIAA Paper* 93-0776.

Hayakawa, K., Smits, A. J. & Bogdonoff, S. M. 1984 Turbulence measurements in a compressible reattaching shear layer. *AIAA J.* **22**, 889–895.

Hayashi, M., Aso, S. & Tan, A. 1989 Fluctuation of heat transfer in shock wave/turbulent boundary layer interaction. *AIAA J.* **27**, 399–404.

Horstman, C. C., Settles, G. S., Williams, D. R. & Bogdonoff, S. M. 1982 A reattaching free shear layer in compressible turbulent flow. *AIAA J.* **20**, 79–85.

Hunt, D. L. & Nixon, D. 1995 A very large eddy simulation of an unsteady shock wave/turbulent boundary layer interaction. *AIAA Paper* 95-2212.

Kistler, A. L. 1964 Fluctuating wall pressure under a separated supersonic flow. *J. Acoust. Soc. Am.* **36**, 543–550.

Kussoy, M. I., Brown, J. D., Brown, J. L., Lockman, W. K. & Horstman, C. C. 1988 Fluctuations and massive separation in three-dimensional shock-wave/boundary-layer interactions. In *Transport Phenomena in Turbulent Flows: Theory, Experiment, and Numerical Simulation* (ed. M. Hirata & N. Kasagi), pp. 875–887. Hemisphere.

Nau, T. 1995 Rayleigh scattering as a quantitative tool in compressible turbulent boundary layers. Master's thesis, Princeton University, Princeton, NJ.

Papamoschou, D. & Roshko, A. 1988 The compressible turbulent shear layer: An experimental study. *J. Fluid Mech.* **197**, 453–477.

Plotkin, K. J. 1975 Shock wave oscillation driven by turbulent boundary-layer fluctuations. *AIAA J.* **13**, 1036–1040.

Poggie, J. 1995 On the control of a compressible, reattaching shear layer. PhD thesis, Princeton University, Princeton, NJ.

Poggie, J. & Smits, A. J. 1996 Quantitative visualization of supersonic flow using Rayleigh scattering. *AIAA Paper* 96-0436.

Poggie, J. & Smits, A. J. 1997 Wavelet analysis of wall-pressure fluctuations in a supersonic blunt-fin flow. *AIAA J.* **35**, 1597–1603.

Samimy, M. & Addy, A. L. 1986 Interaction between two compressible, turbulent free shear layers. *AIAA J.* **24**, 1918–1923.

Samimy, M., Petrie, H. L. & Addy, A. L. 1986 A study of compressible turbulent reattaching free shear layers. *AIAA J.* **24**, 261–267.

Selig, M. S., Andreopoulos, J., Muck, K. C., Dussauge, J. P. & Smits, A. J. 1989 Turbulence structure in a shock wave/turbulent boundary-layer interaction. *AIAA J.* **27**, 862–869.

Settles, G. S., Williams, D. R., Baca, B. K. & Bogdonoff, S. M. 1982 Reattachment of a compressible turbulent free shear layer. *AIAA J.* **20**, 60–67.

Shen, Z.-H., Smith, D. R. & Smits, A. J. 1993 Wall pressure fluctuations in the reattachment region of a supersonic free shear layer. *Exps. Fluids* **14**, 10–16.

Shifen, W. & Qingquan, L. 1992 Hypersonic turbulent separated flow past an unswept circular cylinder on a flat plate. *Acta Aero. Sin.* **10**, 38–44.

Shirinzadeh, B., Hillard, M. E. & Exton, R. J. 1991 Condensation effects on Rayleigh scattering measurements in a supersonic wind tunnel. *AIAA J.* **29**, 242–246.

Smith, D. R., Poggie, J., Konrad, W. & Smits, A. J. 1991 Visualization of the structure of shock wave turbulent boundary layer interactions using Rayleigh scattering. *AIAA Paper* 91-0651.

Smith, K. M. & Dutton, J. C. 1996 Investigation of large-scale structures in supersonic planar base flows. *AIAA J.* **34**, 1146–1152.

Smith, M. W. 1989 Flow visualization in supersonic turbulent boundary layers. PhD thesis, Princeton University, Princeton, NJ.

Spina, E. F. 1988 Organized structures in a supersonic turbulent boundary layer. PhD thesis, Princeton University, Princeton, NJ.

Spina, E. F. & Smits, A. J. 1987 Organized structures in a compressible turbulent boundary layer. *J. Fluid Mech.* **182**, 85–109.

Thomas, A. S. W. 1987 The unsteady characteristics of laminar juncture flow. *Phys. Fluids* **30**, 283–285.

Urbin, G., Knight, D. & Zheltovodov, A. A. 1999 Compressible large eddy simulation using unstructured grid – supersonic turbulent boundary layer and compression corner. *AIAA Paper* 99-0427.

Visbal, M. R. 1991 Structure of laminar juncture flows. *AIAA J.* **29**, 1273–1282.

Wegener, P. P. & Pouring, A. A. 1964 Experiments on condensation of water vapor by homogeneous nucleation in nozzles. *Phys. Fluids* **7**, 352–361.

Wu, P., Lempert, W. R. & Miles, R. B. 2000 Megahertz pulse-burst laser and visualization of shock-wave/boundary-layer interaction. *AIAA J.* **38**, 672–679.